ACS NANO

www.acsnano.org

ARTICLE

Nanophotonic Chiral Sensing: How Does It Actually Work?

Steffen Both, Martin Schäferling, Florian Sterl, Egor A. Muljarov, Harald Giessen, and Thomas Weiss*

Cite This: *ACS Nano* 2022, 16, 2822–2832

Read Online

ACCESS | Metrics & More | Article Recommendations | Supporting Information

ABSTRACT: **Nanophotonic chiral sensing has recently attracted a lot of attention. The idea is to exploit the strong light–matter interaction in nanophotonic resonators to determine the concentration of chiral molecules at ultralow thresholds, which is highly attractive for numerous applications in life science and chemistry. However, a thorough understanding of the underlying interactions is still missing. The theoretical description relies on either simple approximations or on purely numerical approaches. We close this gap and present a general theory of chiral light–matter interactions in arbitrary resonators. Our theory describes the chiral interaction as a perturbation of the resonator modes, also known as resonant states or quasi-normal modes. We observe two dominant contributions: A chirality-induced resonance shift and changes in the modes' excitation and emission efficiencies. Our theory brings deep insights for tailoring and enhancing chiral light–matter interactions. Furthermore, it allows us to predict spectra much more efficiently in comparison to conventional approaches. This is particularly true, as chiral interactions are inherently weak and therefore perturbation theory fits extremely well for this problem.**

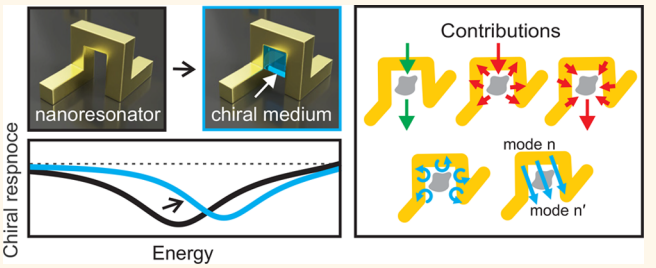

KEYWORDS: *nanophotonics, chirality, sensing, plasmonics, resonant states, quasi-normal modes*

The term "chirality" refers to objects that cannot be superimposed with their mirror image.[1] These two so-called enantiomorphs (or, in case of molecules, enantiomers) differ only in their handedness, which can be left or right. What sounds like a purely mathematical concept has in fact a huge impact, as life itself is chiral.[2,3] The outcome of most biochemical interactions, where chiral biomolecules shake hands, strongly depends on the mutual handedness of the reactants. In extreme examples, the handedness of a molecule makes the difference between a drug and a toxin.[4,5] Therefore, detecting the handedness of molecules is of crucial interest for countless applications in life science and chemistry, as well as for the pharmaceutical industry.[6]

Conventional detection schemes rely on the fact that the interaction of chiral media with light can differ among the two circular polarizations and depends on the handedness of the enantiomers. Assuming a homogeneous and isotropic medium, this interaction is governed by the chiral constitutive equations (below provided in Gaussian units):[7,8]

$$\mathbf{D} = \varepsilon\mathbf{E} - i\kappa\mathbf{H}$$
$$\mathbf{B} = \mu\mathbf{H} + i\kappa\mathbf{E} \qquad (1)$$

Here, the permittivity ε and the permeability μ represent the "nonchiral" properties of the medium, and the Pasteur parameter κ quantifies its chirality. Opposite handedness of the medium results in an opposite sign of κ. A nonzero real part of κ induces a difference in the phase velocities of left- and right-handed circularly polarized light, i.e., circular birefringence, while a nonzero imaginary part induces a difference in their absorption. Measuring this absorption difference—denoted as the circular-dichroism (CD) signal—is the standard method for optically characterizing the chirality of a medium.

Since chiral light–matter interactions are typically extremely weak (at optical frequencies, natural materials have $\kappa \ll 1$), this detection can be very challenging, especially when only tiny amounts of substances are involved. Overcoming this limitation would be highly attractive for numerous applications. A promising approach consists of the use of nanophotonic resonators to boost the chiral light–matter interactions. For the sensing of "nonchiral" material properties, this is already a well-established technique. Applications include the ultrasensitive detection of biomolecules,[9−15]

Received: November 4, 2021
Accepted: January 18, 2022
Published: January 26, 2022

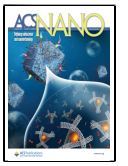

https://doi.org/10.1021/acsnano.1c09796
ACS Nano 2022, 16, 2822–2832

gases,[16,17] and much more.[18−20] In the past decade, a lot of work, both experimental[21−33] and theoretical,[30,34−58] has been carried out to utilize the benefits of this technique for the detecion of chiral substances. Different resonator designs have been investigated, ranging from plasmonic antennas[21−28,38,42] to dielectric nanostructures[29,49,52,54,55] or combinations[50] to so-called "helicity-preserving" cavities.[53,56−58] Another promising route is using structures that exhibit resonances in the ultraviolet region,[31−33] where natural molecules have particularly large κ values. Comprehensive overviews can be found in corresponding review articles.[59−66]

The basic principle of nanophotonic chiral sensing is illustrated in Figure 1(a,b): The starting point is a nanophotonic resonator that can be brought into contact with the chiral medium. The resonator itself may also be chiral (e.g., due to its shape), but it does not have to be. As an example, we depict an array of Ω-shaped plasmonic nanoantennas[67−70] with the chiral medium in their centers. First, the CD spectrum of the resonator without the chiral medium is measured (gray) to serve as a reference. Then, the resonator is brought into contact with the chiral medium and the CD spectrum is measured again (light blue). Note that for visualization, the spectral changes in the plot are dramatically exaggerated. The difference between both spectra (we denote it as ΔCD) contains information about the handedness of the medium. Due to the enhanced light−matter interaction taking place in nanophotonic resonators, the ΔCD signal is typically orders of magnitude larger than the signal that would be obtained from the chiral medium alone.

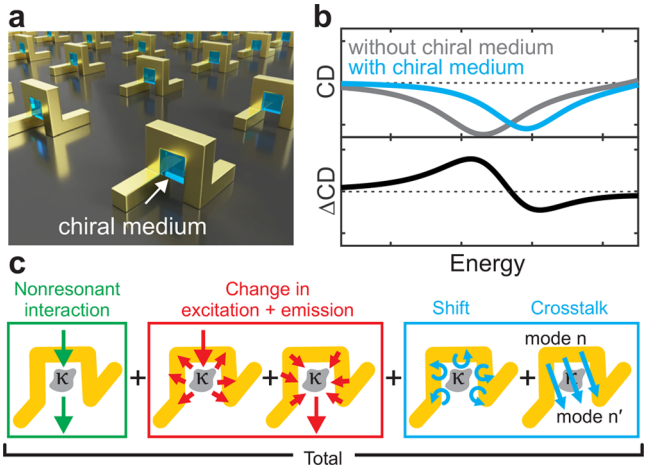

Figure 1. Principle of nanophotonic chiral sensing and underlying contributions. (a) A nanophotonic resonator (example depicts an array of Ω-shaped plasmonic antennas) with a chiral medium in its center. (b) The circular-dichroism (CD) spectrum is measured without (gray) and with (light blue) chiral medium. The change in the spectrum (ΔCD) contains information about the chirality of the medium. (c) As shown in this work, the total interaction can be explained as a combination of five different contributions: A nonresonant interaction, changes in excitation and emission efficiencies of the modes, modal resonance shifts, and intermodal crosstalk. Note that due to similarities that will be discussed later, the contributions are categorized into three different groups.

An important experimental detail in the above procedure is not to use the plain resonator as reference, but rather the resonator covered with a so-called racemic mixture[28,29] (1:1 mixture of left-handed and right-handed enantiomers, which is optically achiral) at the positions where the chiral medium is supposed to be placed later. This ensures that only κ varies between both measurements, while the other material parameters are constant. Note that there also exist variations of the procedure that work without the need to use a racemic mixture;[21,46] however, also in these cases, the key lies in tracing the change of an optical signal induced by the interaction of the resonator with the chiral medium.

For the case of single chiral molecules, the above interaction is well understood;[36,37] however, in practice, one typically does not deal with single chiral molecules, but with chiral media (i.e., a solution or a layer of many molecules). In this case, describing the interaction with a resonator is more sophisticated. The description relies on either simple approximations or purely numerical approaches: The intuitive method[21,30,39,41,44,47,48] consists of evaluating the optical chirality[35] of the resonator's near-field. This allows for predicting the power absorbed in the chiral medium. However, while being very illustrative, this approach has severe limitations:[29,63,71] First, it neglects any influence of the real part of κ, which—albeit would not contribute to the CD of the chiral medium located outside a resonator—is known to strongly contribute to the CD of the combined system.[29,71] Second, it neglects the back action from the chiral medium onto the fields of the resonator, known as induced CD.[37,65,71,72] The rigorous method[27,29,46,51,57,71−75] consists of directly including the chiral medium into numerical calculations via eq 1. However, while this approach accounts for all electromagnetic effects, it provides rather limited insights into the interaction. As an alternative to numerical calculations, in some cases, the interaction can be described analytically via Mie theory[76] or semianalytically via a simple closed-form expression.[49] The former is, however, only applicable for systems with spherical or ellipsoidal symmetry, while the latter only works for resonators that can be treated as an effective medium.

We close the existing gap and present a general theory of chiral light−matter interactions in arbitrary resonators. Our theory retains the rigorousness of the numerical calculations, while at the same time providing a deep intuitive insight. It describes the chiral interaction as a perturbation of the modes of the resonator, also known as resonant states[77−83] or quasi-normal modes.[84−88] We show that the *entire chiral light−matter interaction* can be explained as a combination of five different contributions (illustrated in Figure 1(c)): a nonresonant interaction, changes in the excitation and emission efficiencies of the modes, modal resonance shifts, and intermodal crosstalk. Note that the contributions can be organized into three different categories, due to similarities that will be discussed later. We quantify the impact of these contributions in different sensor geometries. Furthermore, we show that—contrary to common expectation—resonance shifts are often not the dominating source of signal.

Describing nanophotonic resonators via their modes is a highly efficient approach that is experiencing rapidly increasing recognition in the community.[12,20,77−99] Our derivations are based on previous works from the field: In ref 78, a rigorous electrodynamic perturbation method was developed for predicting modal changes in systems containing bianisotropic materials. References 79, 82, and 96 demonstrate how to construct the optical scattering matrix of a resonator from its modes. Based on these works, we have derived a simple

https://doi.org/10.1021/acsnano.1c09796
ACS Nano 2022, 16, 2822−2832

expression for the change of the optical scattering matrix under chiral material perturbations.

RESULTS AND DISCUSSION

Theory. In the following, we give a brief summary of the theory. A detailed derivation can be found in the Supporting Information.[100−104] We start from Maxwell's equations for an optical resonator without any chiral medium. For compactness of notations, we make use of the operator formalism introduced in ref 78. Thus, Maxwell's equations read [Gaussian units, frequency domain, time dependence $\exp(-i\omega t)$, no external currents]:

$$\underbrace{\left[k\begin{pmatrix}\varepsilon(\mathbf{r};\,k) & 0\\ 0 & \mu(\mathbf{r};\,k)\end{pmatrix}-\begin{pmatrix}0 & \nabla\times\\ \nabla\times & 0\end{pmatrix}\right]}_{\hat{\mathbb{M}}(k)}\underbrace{\begin{pmatrix}\mathbf{E}(\mathbf{r})\\ i\mathbf{H}(\mathbf{r})\end{pmatrix}}_{\mathbb{F}}=0 \tag{2}$$

Here, k represents the vacuum wavenumber (for brevity of notations, we will consistently use $k = \omega/c$ instead of the angular frequency ω); the permittivity $\varepsilon(\mathbf{r}; k)$ and permeability $\mu(\mathbf{r}; k)$ describe the spatial material distribution of the resonator, and $\mathbf{E}$ and $\mathbf{H}$ denote the electric and magnetic field, respectively. By combining the fields into a six-dimensional supervector $\mathbb{F}$, and summarizing all other quantities into the Maxwell operator $\hat{\mathbb{M}}$, Maxwell's equations become a simple one-line equation: $\hat{\mathbb{M}}\mathbb{F} = 0$. The modes of the resonator are defined as the solutions of this equation that simultaneously satisfy outgoing boundary conditions. One finds[78]

$$\hat{\mathbb{M}}(k_n)\mathbb{F}_n = 0 \tag{3}$$

where n is an index that labels the modes, $\mathbb{F}_n$ denote the modal field distributions, and k_n are the corresponding wavenumber eigenvalues. In general, k_n are complex, with $\mathrm{Re}(k_n)$ representing the resonance wavenumbers of the modes and $-2\,\mathrm{Im}(k_n)$ denoting their line widths. Since nanophotonic resonators are typically open systems[85] (they leak energy to the environment), their modes are generally referred to as resonant states or quasi-normal modes. For the sake of brevity, we will continue to use the intuitive term modes. Note that eq 3 defines $\mathbb{F}_n$ only up to an arbitrary scalar factor. In order to be applicable for an expansion, they have to be normalized. Valid normalization schemes can be found in refs 77, 78, 82, 85, 86, 95, and references therein.

A very convenient formalism to summarize the interaction of a resonator with incident light is via the optical scattering matrix S.[79,82,96,99] The idea is as follows: The resonator has different so-called incoming channels $\mathbf{N}$, via which it can be excited, and different so-called outgoing channels $\mathbf{M}$, via which it can radiate light.[82,105] Here, the vectors $\mathbf{N}$ and $\mathbf{M}$ each represent a set of quantum numbers that specify details about the respective channel (e.g., polarization, propagation direction). Each element $S_{\mathbf{MN}}$ of the scattering matrix represents the transmission (or reflection) amplitude from one particular input channel $\mathbf{N}$ into one particular output channel $\mathbf{M}$. The scattering matrix can be calculated from the modes as[79,82,96]

$$S_{\mathbf{MN}} = S^{\mathrm{bg}}_{\mathbf{MN}} + \sum_n \frac{a_{n,\mathbf{M}}\,b_{n,\mathbf{N}}}{k-k_n} \tag{4}$$

Here, $S^{\mathrm{bg}}_{\mathbf{MN}}$ corresponds to a nonresonant background term, while $a_{n,\mathbf{M}}$ and $b_{n,\mathbf{N}}$ represent the emission and excitation coefficients, respectively, of the modes $\mathbb{F}_n$ (expressions provided in the Supporting Information). Furthermore, k denotes the wavenumber at which the resonator is excited. Note that $S^{\mathrm{bg}}_{\mathbf{MN}}$, $a_{n,\mathbf{M}}$, and $b_{n,\mathbf{N}}$ are considered here as k dependent. We want to remark that there exist several alternative representations[79,82,96,99] of eq 4, which differ in the definition of the background term and the coefficients.

Now, let us assume the resonator is perturbed by locally inserting a chiral medium. Mathematically, this can be accounted for by changing the operator $\hat{\mathbb{M}}$ that describes the resonator to $\hat{\mathbb{M}} + \delta\hat{\mathbb{M}}$, with the perturbation operator $\delta\hat{\mathbb{M}}$, which is defined as[78]

$$\delta\hat{\mathbb{M}} = \begin{cases} -k\kappa\begin{pmatrix}0 & 1\\ 1 & 0\end{pmatrix} & \text{inside volume } V_c,\\ 0 & \text{outside}\end{cases} \tag{5}$$

Here, V_c represents the volume in which the chiral medium is inserted, and κ is the Pasteur parameter. The above $\delta\hat{\mathbb{M}}$ corresponds to the most relevant scenario, where one transitions from a racemic mixture to a chiral medium, such that only κ varies and the "nonchiral" material parameters ε and μ stay constant. It is straightforward, though, to extend $\delta\hat{\mathbb{M}}$ for changes in ε and μ as well. Furthermore, instead of considering a scalar κ, it is also possible to include bianisotropic contributions, originating, e.g., from molecular alignment effects.[27,75] The most general $\delta\hat{\mathbb{M}}$ can be found in the Supporting Information.

As a consequence of the perturbation, the scattering matrix changes from S to $S + \delta S$, where δS denotes the change. In the case of chiral media, one can safely assume that the perturbation is small compared to the unperturbed material parameters. Therefore, one can apply a first-order perturbation theory. After some derivations (see Supporting Information), we obtain the change of the scattering matrix as

$$\delta S = \delta S^{\mathrm{nr}} + \delta S^{\mathrm{ex}} + \delta S^{\mathrm{em}} + \delta S^{\mathrm{shift}} + \delta S^{\mathrm{cross}} \tag{6}$$

which contains five contributions defined as

$$\delta S^{\mathrm{nr}}_{\mathbf{MN}} = \int_{V_c} ik\kappa(\mathbf{E}^{\mathrm{R}}_{\mathbf{M}}\cdot\mathbf{H}_{\mathbf{N}} + \mathbf{H}^{\mathrm{R}}_{\mathbf{M}}\cdot\mathbf{E}_{\mathbf{N}})\,\mathrm{d}V \tag{7}$$

$$\delta S^{\mathrm{ex}}_{\mathbf{MN}} = -\sum_n \frac{a_{n,\mathbf{M}}\int_{V_c} ik\kappa(\mathbf{E}^{\mathrm{R}}_{n}\cdot\mathbf{H}_{\mathbf{N}} + \mathbf{H}^{\mathrm{R}}_{n}\cdot\mathbf{E}_{\mathbf{N}})\,\mathrm{d}V}{k-k_n} \tag{8}$$

$$\delta S^{\mathrm{em}}_{\mathbf{MN}} = -\sum_n \frac{b_{n,\mathbf{N}}\int_{V_c} ik\kappa(\mathbf{E}^{\mathrm{R}}_{\mathbf{M}}\cdot\mathbf{H}_{n} + \mathbf{H}^{\mathrm{R}}_{\mathbf{M}}\cdot\mathbf{E}_{n})\,\mathrm{d}V}{k-k_n} \tag{9}$$

$$\delta S^{\mathrm{shift}}_{\mathbf{MN}} = \sum_n \frac{a_{n,\mathbf{M}}b_{n,\mathbf{N}}\int_{V_c} ik\kappa(\mathbf{E}^{\mathrm{R}}_{n}\cdot\mathbf{H}_{n} + \mathbf{H}^{\mathrm{R}}_{n}\cdot\mathbf{E}_{n})\,\mathrm{d}V}{(k-k_n)^2} \tag{10}$$

$$\delta S^{\mathrm{cross}}_{\mathbf{MN}} = \sum_{n\neq n'} \frac{a_{n,\mathbf{M}}b_{n',\mathbf{N}}\int_{V_c} ik\kappa(\mathbf{E}^{\mathrm{R}}_{n}\cdot\mathbf{H}_{n'} + \mathbf{H}^{\mathrm{R}}_{n}\cdot\mathbf{E}_{n'})\,\mathrm{d}V}{(k-k_n)(k-k_{n'})} \tag{11}$$

Here, $\mathbf{E}_{\mathbf{M}}$,$\mathbf{H}_{\mathbf{M}}$, and $\mathbf{E}_{\mathbf{N}}$,$\mathbf{H}_{\mathbf{N}}$ denote the background fields belonging to the $\mathbf{M}$th outgoing and the $\mathbf{N}$th incoming channel,

https://doi.org/10.1021/acsnano.1c09796
ACS Nano 2022, 16, 2822−2832

respectively (for details, see Supporting Information), while $\mathbf{E}_n,\mathbf{H}_n$ represent the fields of mode n. The superscript R indicates reciprocal conjugation,[82] which is included for the sake of generality and is, e.g., needed when dealing with periodic systems under oblique incidence angles.[97] In most practically relevant cases (for details, see refs 78, 82, and 96), one trivially obtains $\mathbf{E}^{\mathrm{R}} = \mathbf{E}$ and $\mathbf{H}^{\mathrm{R}} = \mathbf{H}$.

Equations 6 to 11 are the main result of this work. They allow one to predict the response of a resonator to chiral material changes via simple overlap integrals of the unperturbed fields over the region of the perturbation. We want to remark that, although we are only interested in κ changes, the above equations can be easily extended to account for changes in ε, μ, and the bianisotropic parameters as well. The general expressions are provided in the Supporting Information.

As shown above, the total change δS is composed of five contributions. Every contribution describes the effect of a different perturbation-induced physical process on the scattering matrix. The first one, δS^{nr}, contains an overlap integral between incoming and outgoing background fields and represents a nonresonant interaction. The second, δS^{ex}, and third contribution, δS^{em}, consist of overlap integrals of the modes with the background fields, which describe changes in the excitation and emission efficiencies, respectively. The relevance of this overlap has been predicted by us in a previous numerical study.[72] The above equations now rigorously prove this prediction. The fourth contribution, $\delta S^{\mathrm{shift}}$, contains an overlap integral of the modes with themselves, which is associated with a shift of their wavenumber eigenvalues. The fifth contribution, $\delta S^{\mathrm{cross}}$, comprises an overlap integral between different modes, which describes perturbation-induced crosstalk. Note that the shift and the crosstalk contributions are mathematically very similar. Therefore, we categorized them into a common group of effects in the illustrations of Figure 1. We will later investigate the significance of these contributions in different example systems. However, from the above equations, one can already make some general deductions: The nonresonant interaction is independent of the modes and thereby independent of any resonant near-field enhancement. Therefore, it can be expected to be weak, as long as the volume V_c of the chiral medium is not significantly large. Furthermore, in many resonators, the modes are spectrally well separated [mathematically speaking, the difference between $\mathrm{Re}(k_n)$ and $\mathrm{Re}(k_{n'})$ of neighboring modes is larger than their line widths]. In this case, the crosstalk will be weak as well (cf., denominator of eq 11).

Let us now have a closer look at the shift contribution. As already indicated, $\delta S^{\mathrm{shift}}$ denotes the response of the scattering matrix to resonance shifts. The shift of the wavenumber eigenvalue of an individual mode is given as

$$\Delta k_n = \int_{V_c} \underbrace{ik_n\kappa(\mathbf{E}_n^{\mathrm{R}}\cdot\mathbf{H}_n + \mathbf{H}_n^{\mathrm{R}}\cdot\mathbf{E}_n)}_{\text{“}\Delta k_n\text{ per volume”}}\,\mathrm{d}V \tag{12}$$

This is the chiral analogue of the eigenvalue shift that is well-known from previous work on “nonchiral” sensing for ε and μ changes,[20,77,81,84,85,97,98] where it is considered to be the crucial quantity to maximize the sensitivity. The term under the integral can be interpreted as a “shift per volume” density. In general, Δk_n is complex, with $\mathrm{Re}(\Delta k_n)$ corresponding to a change in the resonance wavenumber and $-2\,\mathrm{Im}(\Delta k_n)$ representing a change in the line width.

The above equation reveals an interesting connection to the optical chirality introduced by Tang and Cohen:[35] Let us assume a typical chiral medium with $|\mathrm{Re}(\kappa)| \gg |\mathrm{Im}(\kappa)|$, a resonator with low losses, i.e., $|\mathrm{Re}(k_n)| \gg |\mathrm{Im}(k_n)|$, and furthermore restrict the considerations to a scenario where $\mathbf{E}^{\mathrm{R}} = \mathbf{E}$ and $\mathbf{H}^{\mathrm{R}} = \mathbf{H}$. In this case, one finds that the change of the resonance wavenumber $\mathrm{Re}(\Delta k_n)$ is proportional to the integral over $\mathrm{Im}(\mathbf{E}_n\cdot\mathbf{H}_n)$. This quantity is closely related to the optical chirality. Therefore, as a rule of thumb, one can deduce that systems optimized for strong chiral modes are also sensitive for resonance wavenumber changes.

Example 1: Rod Antennas. In the following, we will apply our theory to different examples of nanoresonator systems. As a first example, we consider one of the most frequently used structures in nanophotonic sensing: an array of plasmonic rod antennas. The geometry is depicted in Figure 2(a). The dimensions are chosen to achieve a resonance in the near-infrared spectral range (for details, see Methods section). The

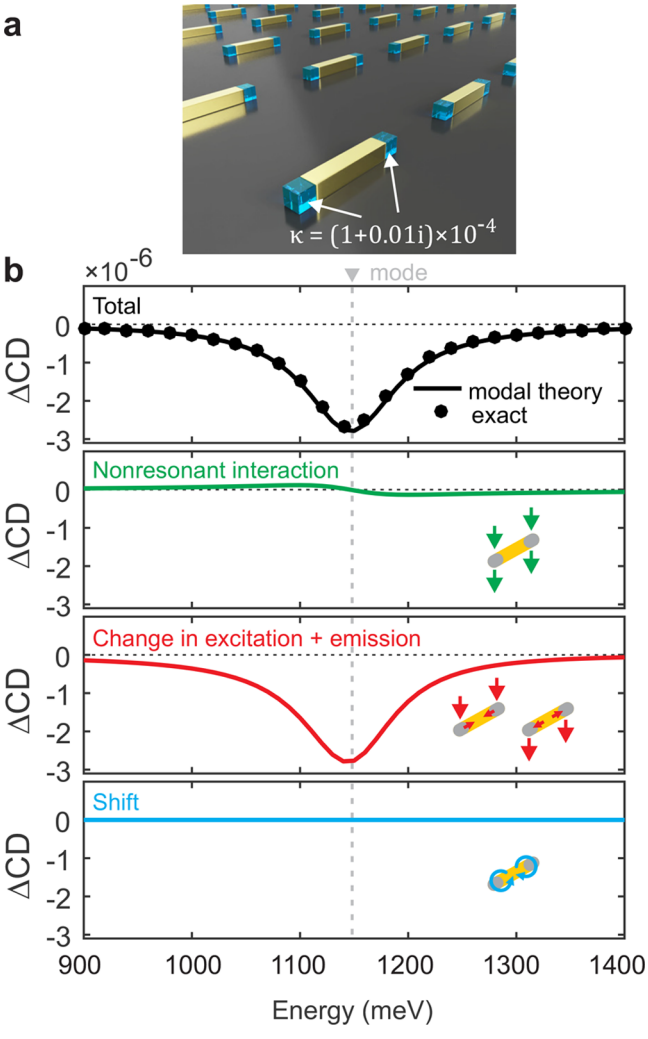

Figure 2. Optical response of plasmonic rod antennas. (a) We consider an array of rod antennas with chiral media patches located at each end. (b) Resulting ΔCD spectrum. The top plot denotes the total signal (line: calculated with our modal theory; dots: exact full-wave calculations). The individual contributions are depicted below. The system is dominated by the changes in the excitation and emission efficiencies, while the shift contribution is exactly zero.

https://doi.org/10.1021/acsnano.1c09796
ACS Nano 2022, 16, 2822−2832

antennas consist of gold and are surrounded by water. Chiral media patches are placed at the ends of each antenna, i.e., in the regions where the strongest near-fields occur. The chiral medium is accounted for with a Pasteur parameter of $\kappa = (1 + 0.01i) \times 10^{-4}$. This value is deliberately chosen such that it exhibits a large but still realistic magnitude[29,106] and contains a typical ratio between real and imaginary part.[29,72]

Figure 2(b) shows the spectral response of the antennas at normal incidence around their fundamental plasmonic mode, which is found at an energy of $1146.1 - 51.3i$ meV. As a representative quantity, we plot the ΔCD signal. The corresponding matrices S and δS with all their components can be found in Figures S1 and S2 of the Supporting Information. Details on how the ΔCD signal is obtained from S and δS are provided in the Supporting Information. The matrices were calculated from inserting the fundamental mode into eqs 4 and 6. To improve the accuracy of S, an additional cubic fit was used as background to account for the influence of higher-order modes (for details, see Methods section).

The top panel in Figure 2(b) depicts the total ΔCD signal. The line denotes the result of the modal theory, while the dots have been obtained by exact full-wave calculations (for details, see Methods section) and are plotted for comparison. It can be seen that there is excellent agreement. The total ΔCD signal exhibits a Lorentzian line shape, with its highest absolute value being located at the resonance energy of the mode (indicated by a vertical dashed line). The lower panels display the different contributions. For compactness, we have summed up the change in the excitation and emission efficiency contributions to one curve. Furthermore, there is no crosstalk curve, since only one mode is considered. Note that the curve for the nonresonant interaction shows a zero crossing at exactly the resonance energy of the mode. This might strike as a mistake, since δS^{nr} does not contain any modal dependence (cf., eq 7). There is, however, a trivial explanation: As already mentioned, we do not look at the contributions of δS, but at their impacts on the ΔCD signal. These impacts contain an additional modulation by the unperturbed scattering matrix S (for details, see derivation of ΔCD in the Supporting Information) and this matrix has a modal dependence.

The results in Figure 2(b) paint a very clear picture: The system is dominated by the change in the excitation and emission efficiencies of the mode. The nonresonant interaction contribution is very small and practically irrelevant. The shift contribution is not only small but turns out to be strictly zero. This result is quite surprising, since resonance shifts are widely believed to be the driving mechanism behind nanophotonic chiral sensing.[21,25,27,38]

In order to understand why the shift contribution is zero, it is instructive to have a closer look at the mode. Its electric field is visualized in Figure 3(a). By applying eq 12, one can derive the corresponding "shift per volume" density. The result is plotted in Figure 3(b). Note that for consistency with the spectra, we use units of energy ("ΔE_n per volume") instead units of wavevector ("Δk_n per volume"). The shift of the energy eigenvalue ΔE_n ($=c\hbar\Delta k_n$) is obtained by integrating the "shift per volume" density over the volume of the perturbation (the chiral media patches are displayed in Figure 3(b) as bluish cubes). From the plot, it is obvious that the integral vanishes: First of all, the "shift per volume" is very weak inside the region of the patches. Second, and more importantly, positive (red) and negative (blue) contributions are occurring symmetrically such that they cancel out each other. It can be easily deduced

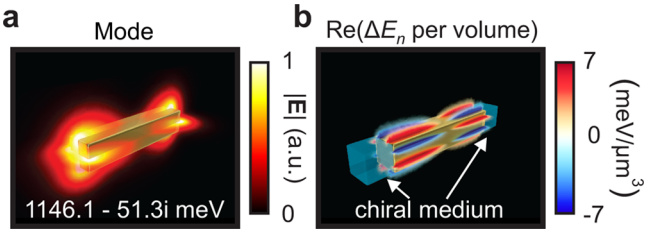

Figure 3. Details on the resonance shift in the rod antennas. (a) Fundamental plasmonic mode. (b) "Shift per volume" of that mode. From the figure, it is obvious that inside the volume of the chiral media patches (displayed in panel (b) as bluish cubes), the "shift per volume" is very weak, and furthermore, positive and negative contributions cancel out each other.

from the plot that this symmetry argument does not only apply when the chiral medium is positioned at the ends of the antenna, but also holds for other distributions, e.g., when the medium would completely surround the antenna.

In fact, it is straightforward to prove that *any geometrically achiral sensor* will experience zero resonance shift in first-order perturbation theory. The argument is as follows: The electric field classifies as a vector (it flips its direction under parity inversion), while the magnetic field classifies as a pseudovector (it does not flip its direction under parity inversion).[107] This makes the shift ΔE_n defined by eq 12 a pseudoscalar (it does change its sign under parity inversion). Now let us suppose that the considered sensor is geometrically achiral. Since geometrically achiral sensors are by definition invariant under parity inversion, one will obtain $\Delta E_n = -\Delta E_n$. The only solution is that $\Delta E_n = 0$. Hence, geometrically achiral sensors cannot exhibit a resonance shift within the limits of first-order perturbation theory.

Since this statement only concerns the first perturbation order, one may wonder if there can appear a shift in higher orders of perturbation. To investigate this, we have calculated the eigenvalues of the rod antenna system as a function of κ, for the case in which $|\kappa|$ becomes extremely large. The results are displayed in Figure S3 of the Supporting Information. We find that, indeed, for very large $|\kappa|$, the eigenvalues start to noticeably change, even in this achiral sensor. Thus, there does exist a higher-order shift. However, it turns out that this higher-order shift is useless for sensing: First, it becomes significant only at extremely large $|\kappa|$ values, which are far beyond what is known for any natural material. Second, and more importantly, for achiral sensors, it is always symmetric with respect to $+\kappa$ and $-\kappa$. To prove this, one simply needs to consider two facts: (a) Replacing $+\kappa$ by $-\kappa$ in an achiral sensor is equivalent to a parity inversion of the perturbed Maxwell operator. (b) Energy eigenvalues must be invariant under parity inversion. In other words: Only even orders of perturbation in κ can yield nonzero resonance shifts, but these are insensitive with respect to the sign of κ. Therefore, the higher-order shift cannot distinguish between the two enantiomers of a chiral molecule.

The above considerations suggest, that it can, however, be possible to enforce a first-order resonance shift in the rod antennas by breaking the achiral symmetry of the patch arrangement. An obvious choice consists of placing the chiral medium only in regions with a uniform sign of the "shift per volume" density.[40] To verify this, we have considered the rod antenna with the chiral medium distributed over the positive regions [red spots in Figure 3(b)]. The results (see Figures S4

https://doi.org/10.1021/acsnano.1c09796
ACS Nano 2022, 16, 2822−2832

and S5 of the Supporting Information) confirm that this arrangement indeed provides a nonzero shift contribution. However, interestingly, it can only be observed in the channels of δS, but not in the ΔCD spectrum, since the signals from different channels cancel out each other. Furthermore, it is quite obvious that such a three-dimensional patch arrangement would be rather difficult to realize in practice.

Example 2: Ω Antennas. Let us now use the insight of our theory to find a system that is particularly designed to feature a strong resonance shift. According to eq 12, there are two requirements: On one hand, the system needs to support a mode with strong collinear electric and magnetic fields in some region of space. On the other hand, the product between both fields should exhibit one predominant sign. Nanophotonics provides a rich pallet of building blocks that can be used to achieve this. In fact, many systems discussed in the literature on chiral sensing[21,38,39,42,44,46] are already optimized for strong optical chirality and—due to the connection discussed under eq 12—should intrinsically meet these requirements. However, as a very intuitive example, let us consider the following: The textbook example for a nanostructure that supports a strong resonant electric field is the plasmonic rod antenna. The textbook example for a nanostructure that supports strong resonant magnetic fields is the split ring resonator. An easy way to combine both is to take an upright standing split-ring resonator and attach two rod antennas to its feet. The result is a structure that looks as the Greek letter Ω, as depicted in Figure 1(a). The particular arrangement of the building blocks promises collinearity of the fields within the center of the Ω. Although they have never been utilized in the context of sensing so far, such Ω antennas are known to exhibit a strong chiroptical far-field response.[67−70] We consider again a periodic array of antennas. The materials are the same as in the previous example, and the dimensions are chosen comparably (for details, see Methods section). Note, however, that the fabrication of such three-dimensional structures is in general not an easy challenge (although there are approaches[69,70,108,109]).

Figure 4(a) displays the "shift per volume" density of the energetically lowest two excitable plasmonic modes. The results confirm what was intuitively expected: There is a hotspot with high uniform values in the center of the antenna. Note that for the given configuration, mode 1 exhibits a negative sign, while mode 2 exhibits a positive one. Let us now assume that a patch of chiral medium is positioned in the hotspot [for visualization, see Figure 1(a)]. Figure 4(b) displays the resulting energy eigenvalue shifts ΔE_n (both the real and imaginary parts) as a function of κ. On the x axis, κ is varied as a multiple of $\kappa_0 = (1 + 0.01i) \times 10^{-4}$. The lines show the prediction of the modal theory, while the dots have been derived from exact full-wave calculations and are depicted for comparison. It is evident that there is an excellent agreement. As expected from the "shift per volume" plots, the energy eigenvalues are very sensitive to κ changes. In agreement with the sign of the "shift per volume" density in the hotspot, mode 1 shows a negative slope in the $\mathrm{Re}(\Delta E_n)$ plot, while mode 2 exhibits a positive one.

To investigate the impact of the ΔE_n shifts, we evaluate again the spectral response of the system. In order to improve the accuracy, we include one further mode in the calculation. This mode is found at an energy eigenvalue of $1750.1 - 25.4i$ meV and contributes to the spectrum via crosstalk. The calculation results are displayed in Figure 5. (Note that for a deeper analysis of the additional mode, the interested reader may find the calculation results with the energy range extended to this mode in Figure S8 of the Supporting Information.) As in the rod antenna example, we depict only the ΔCD signal, while the matrices S and δS can be found in Figures S6 and S7, respectively, of the Supporting Information. All calculations are analogous to the case of the rod antennas, with the only difference that three modes are considered instead of one. As before, we take a fixed value of $\kappa = (1 + 0.01i) \times 10^{-4}$ [cf., Figure 5(a)]. Figure 5(b) (top panel) displays the total ΔCD signal. One can again observe an excellent agreement between the prediction of the modal theory (line) and exact full-wave calculations (dots). Two distinct features can be identified: A peak at the resonance energy of mode 1, and a zero crossing surrounded by large absolute values at the resonance energy of mode 2.

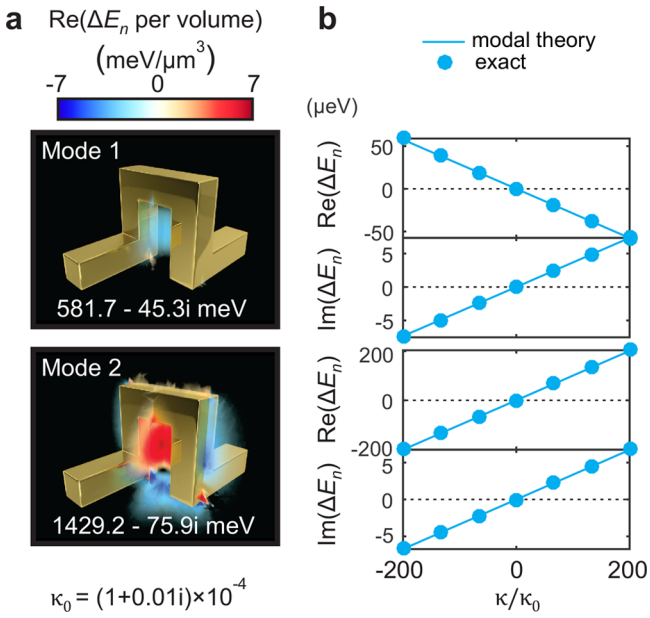

Figure 4. Resonance shift in Ω antennas. The Ω antennas are expected to have a collinear electric and magnetic field at their centers, which results in a nonzero resonance shift. (a) "Shift per volume" of two plasmonic modes. Both modes exhibit hotspots with high values and a uniform sign in the center of the antenna. (b) Change in the energy eigenvalues (lines: modal theory; dots: exact full-wave calculations) of the modes as a function of κ for a chiral medium located at the center of the antenna as shown in Figure 1. The top and bottom plots of each subpanel correspond to the change in the real and imaginary part, respectively.

The lower panels depict the individual contributions, subdivided into their modal origin. As it can be seen, in this system, the shift contribution plays an important role for the total signal. However, in addition, the changes in the excitation and emission efficiencies are also quite strong. One can quantify the importance of the individual contributions for each mode separately: For mode 1, the change in the emission efficiencies is dominating over the shift. This combination leads to the peak shape in the ΔCD spectrum. For mode 2, the shift is dominating over the efficiency changes, leading to the zero-crossing behavior. The contributions associated with mode 3 only play a minor role. The nonresonant interaction is weak as well.

A careful reader may have noticed that modes 1 and 2 show opposite signs of the "shift per volume" density, and their

https://doi.org/10.1021/acsnano.1c09796
ACS Nano 2022, 16, 2822−2832

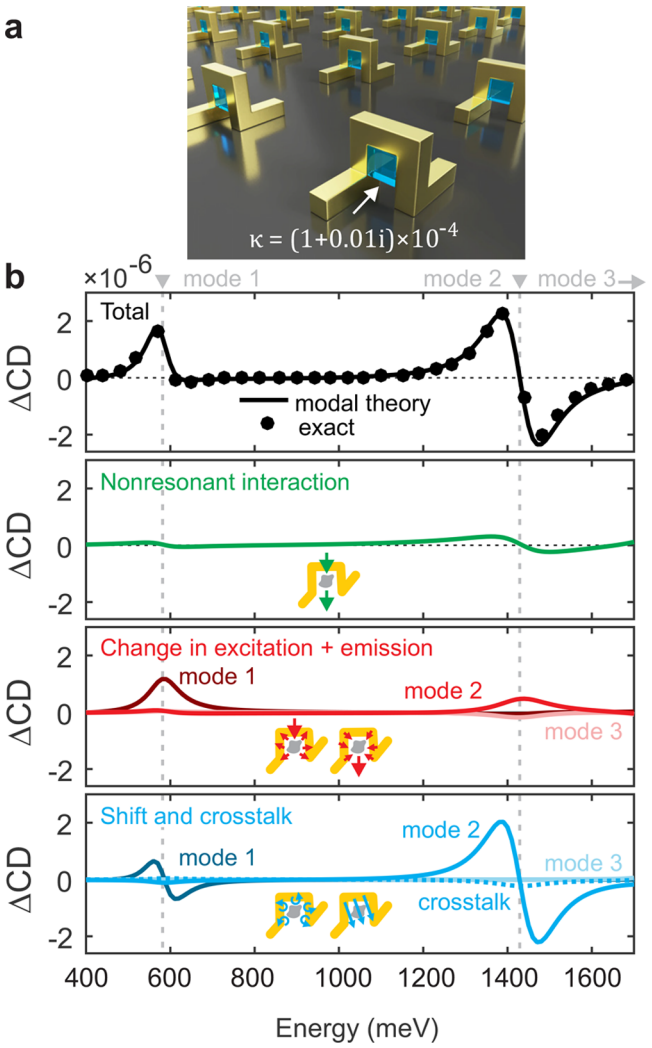

Figure 5. Optical response of the Ω antennas. (a) Array of antennas with chiral media patches in their center. (b) Resulting ΔCD spectrum. The top plot denotes the total signal (line: calculated with our modal theory; dots: exact full-wave calculations). The individual contributions are depicted below. As can be seen, in this system, the change in the excitation and emission efficiencies as well as the shift are all relevant. Around mode 2, the resonance shift is dominant.

resonance energies are shifted in opposite directions by the perturbation (cf., Figure 3), but nevertheless, both provide shift contributions of the same sign to the ΔCD signal. This seems to be a paradox. However, there is a simple explanation: We look at the ΔCD signal, i.e., the change of the CD signal. The CD signal of the unperturbed Ω has a positive peak at mode 1, but a negative peak at mode 2 (cf., Figure S9 of the Supporting Information). Shifting a positive CD peak along one specific direction on the energy axis provides a contribution to ΔCD that has the opposite sign compared to shifting a negative peak along the same direction. Since both peaks are shifted in different directions, the sign of their contribution to ΔCD is the same.

To summarize the findings of the Ω example: This example demonstrates that it is indeed possible to design a sensor with large resonance shifts. However, interestingly, even in this sensor, the relevance of the changes in the excitation and emission efficiencies should not be underestimated. We do not see any reason that this should be different for other structures optimized for strong chiral near-fields. Thus, while an analysis of optical chirality can yield promising nanostructure designs for sensing applications, all contributions must be taken into account for sensor optimization.

Further Discussions. After considering these two example systems, one might wonder which one has the better overall performance. Therefore, we evaluated their CD enhancement factors[72] (defined as |ΔCD| of the system normalized to the |CD| of the chiral patches without the antennas). The results are depicted in Figure S10 of the Supporting Information. The answer might appear rather surprising: The rod antennas exhibit a maximum value of 325 and thereby outperform the Ω antennas, which only provide a maximum value of 250. Another advantage of the rod antennas is that, since they are geometrically achiral, they do not provide any CD signal in the absence of the chiral medium.[34]

In accordance with a previous numerical study,[72] our results suggest that changes in the excitation and emission efficiencies (related to strong overlap of the incident fields with the modes) have to be considered as a relevant mechanism for nanophotonic chiral sensing rather than resonance shifts (related to strong overlap between the modes' electric and magnetic fields). Furthermore, our derivations reveal that in general, stronger near-fields—regardless of with or without high optical chirality—lead to larger signals. There is no need for designing systems such that they exhibit a strong optical chirality with simultaneously weak electric fields, as suggested in early works.[35,110] The difference is that these early works focused on optimizing a quantity known as enantioselectivity and not the absolute signal strength, which, however, denotes the relevant factor that defines the signal-to-noise ratio and consequently the detection thresholds in the majority of optical sensors.[16]

Concerning the detection thresholds, one should be aware that the absolute values of the ΔCD signal reported in this article are quite low and roughly 1 order of magnitude below the detection limit of most commercial CD spectrometers.[34,72] The low ΔCD values stem from the small amount of chiral medium per unit area of the periodic system that was used in our examples, in order to keep them simple. Comparable systems, but with a larger amount of chiral medium inserted, have been shown to provide absolute signal strengths well above the detection limit.[28,29] In our case, a larger amount of chiral medium per unit area can be achieved by using either a higher density of antennas or by covering the antennas completely with the chiral medium instead of only their ends or centers, respectively.

All considerations made in this work are based on a first-order approximation in κ. Therefore, it is quite natural to ask what the limitations of this approach are. To systematically investigate the validity range of the theory, we have varied κ over many orders of magnitude and compared the predicted ΔCD spectra to exact full-wave calculations. Negative signs were considered as well. The results are depicted in Figure S11 of the Supporting Information. They reveal that the first-order approximation is accurate over a surprisingly huge range of values. Only when the order of $|\kappa|$ approaches unity do the deviations become relevant. Such values would be, however, far beyond what is known for any natural material.

Let us add some further remarks on the overall applicability of our method: In systems that have a lot of modes within (or around) the energy range of interest, the modal approach may

https://doi.org/10.1021/acsnano.1c09796
ACS Nano 2022, 16, 2822−2832

become impractical. The reason is that in general, all those modes have to be considered in the calculation, in order to obtain accurate results. Furthermore, in periodic systems, energies around the Rayleigh anomalies[111] are problematic, since these anomalies also effectively act as an ensemble of modes.[94,102]

In the end, we want to point out a benefit of the modal theory that was not mentioned so far and becomes relevant when calculating spectra for different κ values: While conventional full-wave simulations have to be repeated multiple times, the modal theory allows to predict the output over the whole range of κ values with one single calculation. This is possible, because κ appears as a linear factor in the integrals of δS [see eqs 6−11]. Therefore, one only has to evaluate the integrals with κ factored out and can multiply the result with any complex value of interest, to directly obtain the desired spectra. This even works when κ is not constant, but dispersive. There are at least two applications in sensor modeling: First, one is often interested in the sensor response to different analyte media. Second, even for one particular chiral analyte, one is typically interested in the response to both of its enantiomers (i.e., to both values $\pm\kappa$). Related to sensor modeling, there is a further benefit of the perturbative approach: It should not be forgotten that realistic κ values are typically extremely small. In full-wave calculations, this sets high standards for the accuracy of the simulations, so that the relevant signals do not vanish within numerical noise.[51,72] The smaller the value of κ gets, the more computationally expensive the numerical simulation becomes. In sharp contrast, the perturbative approach can effortlessly predict spectral changes for *arbitrarily* small values of κ.

CONCLUSIONS

We have presented a general theory of chiral light−matter interactions in nanophotonic resonators. Our theory reveals the mechanisms behind nanophotonic chiral sensing. There are exactly five contributions: a nonresonant interaction, changes in the excitation and emission efficiencies of the resonator modes, modal resonance shifts, and intermodal crosstalk. We have investigated the impact of these contributions in different sensor geometries. We have demonstrated that—contrary to common expectations—resonance shifts are often not the dominating source of signal. In the case of achiral sensors, they are even strictly zero in first order. Instead, it turns out that the changes in the excitation and emission efficiencies can be the driving mechanism for enhancing circular dichroism spectroscopy. Besides enabling deep intuitive insights for the understanding and tailoring of nanophotonic chiral light−matter interactions, our theory also constitutes a highly efficient computational tool, with clear advantages over conventional approaches in terms of calculation time and efforts.

METHODS

Calculations. All calculations were performed using the commercial finite-element solver COMSOL Multiphysics. The chiral constitutive equations were implemented according to ref 72. The modes were calculated and normalized following the method provided in ref 86. The gold dielectric function was described by a Drude model with plasma frequency $\omega_p = 1.37 \times 10^{16}$ rad/s and a damping constant $\gamma = 1.22 \times 10^{14}$ rad/s (adopted from ref 112). The water was accounted for with its refractive index of 1.33. Calculations have been cross-checked by an in-house implementation of the Fourier-modal method.[113]

Antenna Dimensions. Rod antennas: The rods have a length of 200 nm, a width of 40 nm, and a height of 40 nm, and are periodically arranged in a square lattice with a period of 600 nm. The sizes of the chiral media patches are $40 \times 40 \times 40$ nm^3. Ω antennas: The Ωs have a total length of 240 nm, a total width of 140 nm, and a total height of 140 nm. They are wound of a quadratic wire with a lateral extension of 40 nm. The chiral media patches in their centers are 40 nm in length, 60 nm in width, and 60 nm in height. The Ωs are arranged in a square lattice with a period of 500 nm.

Unperturbed Scattering Matrix. To improve the accuracy of the unperturbed scattering matrix S, the influence of higher-order modes in eq 4 was accounted for with a cubic fit, following the method provided in ref 82. The fit was evaluated at four energy points, equidistantly distributed over the depicted spectral range. Note that S is only needed for the calculation of the ΔCD spectra (see equations in the Supporting Information), while for predicting the change δS, which constitutes the main result of this work, it is not required at all.

Visualization. The fields and the "shift per volume" densities were displayed on selectively chosen slices through the antennas. The slice plots were generated from simulation data and then incorporated into a three-dimensional model of the structure, which had been created with the open-source graphics suite Blender. The transparency (alpha channel) of each slice plot is proportional to the magnitude of the displayed value. The slice positions were selected such that all relevant features are visible: For the field plot of the rod antenna, the slices are at half of the antenna's width and height; for the corresponding "shift per volume" plot, they are at one-quarter and three-quarters of the antenna's width and height; for the plots of the Ω antenna, they are at half the Ω's width and length.

ASSOCIATED CONTENT

Supporting Information

The Supporting Information is available free of charge at https://pubs.acs.org/doi/10.1021/acsnano.1c09796.

Supporting Figures: Scattering matrices of the two example systems; Numerical example for higher-order shift in the rod antennas; Calculations for the rod antennas with the chiral medium distributed over chiral hotspots; Details about mode 3 of the Ω antennas; CD spectrum of the Ω antennas; CD enhancement-factor comparison of the two example systems; Numerical test of the validity range of the first-order approximation. Supporting Notes: Detailed derivation of the modal theory; Details on how the ΔCD signals are calculated from the scattering matrices (PDF)

AUTHOR INFORMATION

Corresponding Author

Thomas Weiss − *4th Physics Institute and Research Center SCoPE, University of Stuttgart, 70569 Stuttgart, Germany; Institute of Physics, University of Graz, and NAWI Graz, 8010 Graz, Austria;* orcid.org/0000-0002-4991-6779; Email: thomas.weiss@uni-graz.at

Authors

Steffen Both − *4th Physics Institute and Research Center SCoPE, University of Stuttgart, 70569 Stuttgart, Germany;* orcid.org/0000-0002-2050-6952

Martin Schäferling − *4th Physics Institute and Research Center SCoPE, University of Stuttgart, 70569 Stuttgart, Germany*

Florian Sterl − *4th Physics Institute and Research Center SCoPE, University of Stuttgart, 70569 Stuttgart, Germany;* orcid.org/0000-0002-1025-6777

Egor A. Muljarov − *Cardiff University, School of Physics and Astronomy, CF24 3AA Cardiff, United Kingdom*
Harald Giessen − *4th Physics Institute and Research Center SCoPE, University of Stuttgart, 70569 Stuttgart, Germany*

Complete contact information is available at: https://pubs.acs.org/10.1021/acsnano.1c09796

Author Contributions

The manuscript was written through contributions of all authors. All authors have given approval to the final version of the manuscript.

Notes

Note that prior to submission, a preprint version of this article had been made available as Both, S.; Schäferling, M.; Sterl, F.; Muljarov, E. A.; Giessen, H.; Weiss, T. Nanophotonic Chiral Sensing: How does it Actually Work? *arXiv*, 2106.15699. https://arxiv.org/abs/2106.15699 (last accessed January 17, 2022)

The authors declare no competing financial interest.

ACKNOWLEDGMENTS

We acknowledge support from the Deutsche Forschungsgemeinschaft (DFG) via the priority program SPP 1834 "Tailored disorder," the research training group GRK 2642 "Towards Graduate Experts in Photonic Quantum Technologies," as well as the individual DFG research grant WE 5815/5-1.

REFERENCES

(1) Kelvin, W. T. *Baltimore Lectures on Molecular Dynamics and the Wave Theory of Light*; CJ Clay and Sons: London, 1904.
(2) Meierhenrich, U. *Amino Acids and the Asymmetry of Life Caught in the Act of Formation*; Advances in astrobiology and biogeophysics; Springer: Berlin, 2008.
(3) Siegel, J. S. Single-handed cooperation. *Nature* **2001**, *409*, 777−778.
(4) Nguyen, L. A.; He, H.; Pham-Huy, C. Chiral Drugs: an Overview. *International journal of biomedical science: IJBS* **2006**, *2*, 85−100.
(5) Aronson, J. *Meyler's Side Effects of Drugs: The International Encyclopedia of Adverse Drug Reactions and Interactions*; ISSN; Elsevier Science: Amsterdam, 2015.
(6) Nina Berova, K. N.; Woody, R. W. *Circular Dichroism. Principles and Applications*, 2nd ed.; Wiley-VCH: New York, 2000.
(7) Lindell, I.; Sihvola, A.; Tretyakov, S.; Viitanen, A. *Electromagnetic Waves in Chiral and Bi-isotropic Media*; Artech House: Boston, 1994.
(8) Sihvola, A. H.; Lindell, I. V. BI-Isotropic Constitutive Relations. *Microwave and Optical Technology Letters* **1991**, *4*, 295−297.
(9) Wilson, W. D. Analyzing Biomolecular Interactions. *Science* **2002**, *295*, 2103−2105.
(10) Liu, N.; Weiss, T.; Mesch, M.; Langguth, L.; Eigenthaler, U.; Hirscher, M.; Sönnichsen, C.; Giessen, H. Planar Metamaterial Analogue of Electromagnetically Induced Transparency for Plasmonic Sensing. *Nano Lett.* **2010**, *10*, 1103−1107.
(11) Liu, N.; Mesch, M.; Weiss, T.; Hentschel, M.; Giessen, H. Infrared Perfect Absorber and Its Application As Plasmonic Sensor. *Nano Lett.* **2010**, *10*, 2342−2348.
(12) Arnold, S.; Khoshsima, M.; Teraoka, I.; Holler, S.; Vollmer, F. Shift of Whispering-Gallery Modes in Microspheres by Protein Adsorption. *Opt. Lett.* **2003**, *28*, 272−274.
(13) Rosman, C.; Prasad, J.; Neiser, A.; Henkel, A.; Edgar, J.; Sönnichsen, C. Multiplexed Plasmon Sensor for Rapid Label-Free Analyte Detection. *Nano Lett.* **2013**, *13*, 3243−3247.
(14) Cetin, A. E.; Coskun, A. F.; Galarreta, B. C.; Huang, M.; Herman, D.; Ozcan, A.; Altug, H. Handheld High-Throughput Plasmonic Biosensor Using Computational On-Chip Imaging. *Light: Sci. Appl.* **2014**, *3*, e122.
(15) Semenyshyn, R.; Hentschel, M.; Stanglmair, C.; Teutsch, T.; Tarin, C.; Pacholski, C.; Giessen, H.; Neubrech, F. In Vitro Monitoring Conformational Changes of Polypeptide Monolayers Using Infrared Plasmonic Nanoantennas. *Nano Lett.* **2019**, *19*, 1−7.
(16) Sterl, F.; Strohfeldt, N.; Both, S.; Herkert, E.; Weiss, T.; Giessen, H. Design Principles for Sensitivity Optimization in Plasmonic Hydrogen Sensors. *ACS Sensors* **2020**, *5*, 917−927.
(17) Pohl, T.; Sterl, F.; Strohfeldt, N.; Giessen, H. Optical Carbon Dioxide Detection in the Visible Down to the Single Digit ppm Range Using Plasmonic Perfect Absorbers. *ACS Sensors* **2020**, *5*, 2628−2635.
(18) Gallinet, B.; Martin, O. J. F. Refractive Index Sensing with Subradiant Modes: A Framework To Reduce Losses in Plasmonic Nanostructures. *ACS Nano* **2013**, *7*, 6978−6987.
(19) Prasad, J.; Zins, I.; Branscheid, R.; Becker, J.; Koch, A. H. R.; Fytas, G.; Kolb, U.; Sönnichsen, C. Plasmonic Core−Satellite Assemblies as Highly Sensitive Refractive Index Sensors. *J. Phys. Chem. C* **2015**, *119*, 5577−5582.
(20) Mesch, M.; Weiss, T.; Schäferling, M.; Hentschel, M.; Hegde, R. S.; Giessen, H. Highly Sensitive Refractive Index Sensors with Plasmonic Nanoantennas-Utilization of Optimal Spectral Detuning of Fano Resonances. *ACS Sensors* **2018**, *3*, 960−966.
(21) Hendry, E.; Carpy, T.; Johnston, J.; Popland, M.; Mikhaylovskiy, R. V.; Lapthorn, A. J.; Kelly, S. M.; Barron, L. D.; Gadegaard, N.; Kadodwala, M. Ultrasensitive Detection and Characterization of Biomolecules Using Superchiral Fields. *Nat. Nanotechnol.* **2010**, *5*, 783−787.
(22) Maoz, B. M.; Chaikin, Y.; Tesler, A. B.; Bar Elli, O.; Fan, Z.; Govorov, A. O.; Markovich, G. Amplification of Chiroptical Activity of Chiral Biomolecules by Surface Plasmons. *Nano Lett.* **2013**, *13*, 1203−1209.
(23) Lu, F.; Tian, Y.; Liu, M.; Su, D.; Zhang, H.; Govorov, A. O.; Gang, O. Discrete Nanocubes as Plasmonic Reporters of Molecular Chirality. *Nano Lett.* **2013**, *13*, 3145−3151.
(24) Wang, R.-Y.; Wang, P.; Liu, Y.; Zhao, W.; Zhai, D.; Hong, X.; Ji, Y.; Wu, X.; Wang, F.; Zhang, D.; Zhang, W.; Liu, R.; Zhang, X. Experimental Observation of Giant Chiroptical Amplification of Small Chiral Molecules by Gold Nanosphere Clusters. *J. Phys. Chem. C* **2014**, *118*, 9690−9695.
(25) Tullius, R.; Karimullah, A. S.; Rodier, M.; Fitzpatrick, B.; Gadegaard, N.; Barron, L. D.; Rotello, V. M.; Cooke, G.; Lapthorn, A.; Kadodwala, M. Superchiral" Spectroscopy: Detection of Protein Higher Order Hierarchical Structure with Chiral Plasmonic Nanostructures. *J. Am. Chem. Soc.* **2015**, *137*, 8380−8383.
(26) Zhao, Y.; Askarpour, A. N.; Sun, L.; Shi, J.; Li, X.; Alù, A. Chirality Detection of Enantiomers Using Twisted Pptical Metamaterials. *Nat. Commun.* **2017**, *8*, 14180.
(27) Kelly, C.; Tullius, R.; Lapthorn, A. J.; Gadegaard, N.; Cooke, G.; Barron, L. D.; Karimullah, A. S.; Rotello, V. M.; Kadodwala, M. Chiral Plasmonic Fields Probe Structural Order of Biointerfaces. *J. Am. Chem. Soc.* **2018**, *140*, 8509−8517.
(28) García-Guirado, J.; Svedendahl, M.; Puigdollers, J.; Quidant, R. Enantiomer-Selective Molecular Sensing Using Racemic Nanoplasmonic Arrays. *Nano Lett.* **2018**, *18*, 6279−6285.
(29) García-Guirado, J.; Svedendahl, M.; Puigdollers, J.; Quidant, R. Enhanced Chiral Sensing with Dielectric Nanoresonators. *Nano Lett.* **2020**, *20*, 585−591.
(30) Poulikakos, L. V.; Gutsche, P.; McPeak, K. M.; Burger, S.; Niegemann, J.; Hafner, C.; Norris, D. J. Optical Chirality Flux as a Useful Far-Field Probe of Chiral Near Fields. *ACS Photonics* **2016**, *3*, 1619−1625.
(31) McPeak, K. M.; van Engers, C. D.; Bianchi, S.; Rossinelli, A.; Poulikakos, L. V.; Bernard, L.; Herrmann, S.; Kim, D. K.; Burger, S.; Blome, M.; Jayanti, S. V.; Norris, D. J. Ultraviolet Plasmonic Chirality from Colloidal Aluminum Nanoparticles Exhibiting Charge-Selective Protein Detection. *Adv. Mater.* **2015**, *27*, 6244−6250.

(32) Jeong, H.-H.; Mark, A. G.; Fischer, P. Magnesium Plasmonics for UV Applications and Chiral Sensing. *Chem. Commun.* **2016**, *52*, 12179−12182.
(33) Kilic, U.; Hilfiker, M.; Ruder, A.; Feder, R.; Schubert, E.; Schubert, M.; Argyropoulos, C. Broadband Enhanced Chirality with Tunable Response in Hybrid Plasmonic Helical Metamaterials. *Adv. Funct. Mater.* **2021**, *31*, 2010329.
(34) Schäferling, M. *Chiral Nanophotonics: Chiral Optical Properties of Plasmonic Systems*; Springer: Cham, 2016.
(35) Tang, Y.; Cohen, A. E. Optical Chirality and Its Interaction with Matter. *Phys. Rev. Lett.* **2010**, *104*, 163901.
(36) Govorov, A. O.; Fan, Z.; Hernandez, P.; Slocik, J. M.; Naik, R. R. Theory of Circular Dichroism of Nanomaterials Comprising Chiral Molecules and Nanocrystals: Plasmon Enhancement, Dipole Interactions, and Dielectric Effects. *Nano Lett.* **2010**, *10*, 1374−1382.
(37) Govorov, A. O. Plasmon-Induced Circular Dichroism of a Chiral Molecule in the Vicinity of Metal Nanocrystals. Application to Various Geometries. *J. Phys. Chem. C* **2011**, *115*, 7914−7923.
(38) Hendry, E.; Mikhaylovskiy, R. V.; Barron, L. D.; Kadodwala, M.; Davis, T. J. Chiral Electromagnetic Fields Generated by Arrays of Nanoslits. *Nano Lett.* **2012**, *12*, 3640−3644.
(39) Schäferling, M.; Dregely, D.; Hentschel, M.; Giessen, H. Tailoring Enhanced Optical Chirality: Design Principles for Chiral Plasmonic Nanostructures. *Phys. Rev. X* **2012**, *2*, 031010.
(40) Schäferling, M.; Yin, X.; Giessen, H. Formation of Chiral Fields in a Symmetric Environment. *Opt. Express* **2012**, *20*, 26326−26336.
(41) García-Etxarri, A.; Dionne, J. A. Surface-Enhanced Circular Dichroism Spectroscopy Mediated by Nonchiral Nanoantennas. *Phys. Rev. B* **2013**, *87*, 235409.
(42) Davis, T. J.; Hendry, E. Superchiral Electromagnetic Fields Created by Surface Plasmons in Nonchiral Metallic Nanostructures. *Phys. Rev. B* **2013**, *87*, 085405.
(43) Davis, T. J.; Gómez, D. E. Interaction of Localized Surface Plasmons with Chiral Molecules. *Phys. Rev. B* **2014**, *90*, 235424.
(44) Schäferling, M.; Yin, X.; Engheta, N.; Giessen, H. Helical Plasmonic Nanostructures as Prototypical Chiral Near-Field Sources. *ACS Photonics* **2014**, *1*, 530−537.
(45) Wu, T.; Ren, J.; Wang, R.; Zhang, X. Competition of Chiroptical Effect Caused by Nanostructure and Chiral Molecules. *J. Phys. Chem. C* **2014**, *118*, 20529−20537.
(46) Schäferling, M.; Engheta, N.; Giessen, H.; Weiss, T. Reducing the Complexity: Enantioselective Chiral Near-Fields by Diagonal Slit and Mirror Configuration. *ACS Photonics* **2016**, *3*, 1076−1084.
(47) Poulikakos, L. V.; Thureja, P.; Stollmann, A.; De Leo, E.; Norris, D. J. Chiral Light Design and Detection Inspired by Optical Antenna Theory. *Nano Lett.* **2018**, *18*, 4633−4640.
(48) Poulikakos, L. V.; Dionne, J. A.; García-Etxarri, A. Optical Helicity and Optical Chirality in Free Space and in the Presence of Matter. *Symmetry* **2019**, *11*, 1113.
(49) Mohammadi, E.; Tsakmakidis, K. L.; Askarpour, A. N.; Dehkhoda, P.; Tavakoli, A.; Altug, H. Nanophotonic Platforms for Enhanced Chiral Sensing. *ACS Photonics* **2018**, *5*, 2669−2675.
(50) Mohammadi, E.; Tittl, A.; Tsakmakidis, K. L.; Raziman, T. V.; Curto, A. G. Dual Nanoresonators for Ultrasensitive Chiral Detection. *ACS Photonics* **2021**, *8*, 1754−1762.
(51) Lee, S.; Kang, J.-H.; Yoo, S.; Park, Q.-H. Robust Numerical Evaluation of Circular Dichroism from Chiral Medium/Nanostructure Coupled Systems Using the Finite-Element Method. *Sci. Rep.* **2018**, *8*, 8406.
(52) Solomon, M. L.; Hu, J.; Lawrence, M.; García-Etxarri, A.; Dionne, J. A. Enantiospecific Optical Enhancement of Chiral Sensing and Separation with Dielectric Metasurfaces. *ACS Photonics* **2019**, *6*, 43−49.
(53) Graf, F.; Feis, J.; Garcia-Santiago, X.; Wegener, M.; Rockstuhl, C.; Fernandez-Corbaton, I. Achiral, Helicity Preserving, and Resonant Structures for Enhanced Sensing of Chiral Molecules. *ACS Photonics* **2019**, *6*, 482−491.
(54) Droulias, S.; Bougas, L. Absolute Chiral Sensing in Dielectric Metasurfaces Using Signal Reversals. *Nano Lett.* **2020**, *20*, 5960−5966.
(55) Lasa-Alonso, J.; Abujetas, D. R.; Nodar, l.; Dionne, J. A.; Sáenz, J. J.; Molina-Terriza, G.; Aizpurua, J.; García-Etxarri, A. Surface-Enhanced Circular Dichroism Spectroscopy on Periodic Dual Nanostructures. *ACS Photonics* **2020**, *7*, 2978−2986.
(56) Feis, J.; Beutel, D.; Köpfler, J.; Garcia-Santiago, X.; Rockstuhl, C.; Wegener, M.; Fernandez-Corbaton, I. Helicity-Preserving Optical Cavity Modes for Enhanced Sensing of Chiral Molecules. *Phys. Rev. Lett.* **2020**, *124*, 033201.
(57) Scott, P.; Garcia-Santiago, X.; Beutel, D.; Rockstuhl, C.; Wegener, M.; Fernandez-Corbaton, I. On Enhanced Sensing of Chiral Molecules in Optical Cavities. *Applied Physics Reviews* **2020**, *7*, 041413.
(58) Beutel, D.; Scott, P.; Wegener, M.; Rockstuhl, C.; Fernandez-Corbaton, I. Enhancing the Optical Rotation of Chiral Molecules Using Helicity Preserving All-Dielectric Metasurfaces. *Appl. Phys. Lett.* **2021**, *118*, 221108.
(59) Govorov, A. O.; Gun'ko, Y. K.; Slocik, J. M.; Gérard, V. A.; Fan, Z.; Naik, R. R. Chiral Nanoparticle Assemblies: Circular Dichroism, Plasmonic Interactions, and Exciton Effects. *J. Mater. Chem.* **2011**, *21*, 16806−16818.
(60) Ben-Moshe, A.; Maoz, B. M.; Govorov, A. O.; Markovich, G. Chirality and Chiroptical Effects in Inorganic Nanocrystal Systems with Plasmon and Exciton Resonances. *Chem. Soc. Rev.* **2013**, *42*, 7028−7041.
(61) Hentschel, M.; Schäferling, M.; Duan, X.; Giessen, H.; Liu, N. Chiral Plasmonics. *Science Advances* **2017**, *3*, e1602735.
(62) Qiu, M.; Zhang, L.; Tang, Z.; Jin, W.; Qiu, C.-W.; Lei, D. 3D Metaphotonic Nanostructures with Intrinsic Chirality. *Adv. Funct. Mater.* **2018**, *28*, 1803147.
(63) Yoo, S.; Park, Q.-H. Metamaterials and Chiral Sensing: a Review of Fundamentals and Applications. *Nanophotonics* **2019**, *8*, 249−261.
(64) Solomon, M. L.; Saleh, A. A. E.; Poulikakos, L. V.; Abendroth, J. M.; Tadesse, L. F.; Dionne, J. A. Nanophotonic Platforms for Chiral Sensing and Separation. *Acc. Chem. Res.* **2020**, *53*, 588−598.
(65) Cao, Z.; Gao, H.; Qiu, M.; Jin, W.; Deng, S.; Wong, K.-Y.; Lei, D. Chirality Transfer from Sub-Nanometer Biochemical Molecules to Sub-Micrometer Plasmonic Metastructures: Physiochemical Mechanisms, Biosensing, and Bioimaging Opportunities. *Adv. Mater.* **2020**, *32*, 1907151.
(66) Kakkanattu, A.; Eerqing, N.; Ghamari, S.; Vollmer, F. Review of Optical Sensing and Manipulation of Chiral Molecules and Nanostructures with the Focus on Plasmonic Enhancements [Invited]. *Opt. Express* **2021**, *29*, 12543−12579.
(67) Tretyakov, S. A.; Mariotte, F.; Simovski, C. R.; Kharina, T. G.; Heliot, J. Analytical Antenna Model for Chiral Scatterers: Comparison with Numerical and Experimental Data. *IEEE Transactions on Antennas and Propagation* **1996**, *44*, 1006−1014.
(68) Rockstuhl, C.; Menzel, C.; Paul, T.; Lederer, F. Optical Activity in Chiral Media Composed of Three-Dimensional Metallic Meta-Atoms. *Phys. Rev. B* **2009**, *79*, 035321.
(69) Helgert, C.; Pshenay-Severin, E.; Falkner, M.; Menzel, C.; Rockstuhl, C.; Kley, E.-B.; Tünnermann, A.; Lederer, F.; Pertsch, T. Chiral Metamaterial Composed of Three-Dimensional Plasmonic Nanostructures. *Nano Lett.* **2011**, *11*, 4400−4404.
(70) Sakellari, I.; Yin, X.; Nesterov, M. L.; Terzaki, K.; Xomalis, A.; Farsari, M. 3D Chiral Plasmonic Metamaterials Fabricated by Direct Laser Writing: The Twisted Omega Particle. *Advanced Optical Materials* **2017**, *5*, 1700200.
(71) Lee, S.; Yoo, S.; Park, Q.-H. Microscopic Origin of Surface-Enhanced Circular Dichroism. *ACS Photonics* **2017**, *4*, 2047−2052.
(72) Nesterov, M. L.; Yin, X.; Schäferling, M.; Giessen, H.; Weiss, T. The Role of Plasmon-Generated Near Fields for Enhanced Circular Dichroism Spectroscopy. *ACS Photonics* **2016**, *3*, 578−583.

https://doi.org/10.1021/acsnano.1c09796
ACS Nano 2022, 16, 2822−2832

(73) Onishi, M.; Crabtree, K.; Chipman, R. A. Formulation of Rigorous Coupled-Wave Theory for Gratings in Bianisotropic Media. *J. Opt. Soc. Am. A* **2011**, *28*, 1747−1758.
(74) Klimov, V.; Zabkov, I.; Pavlov, A.; Guzatov, D. Eigen Oscillations of a Chiral Sphere and Their Influence on Radiation of Chiral Molecules. *Opt. Express* **2014**, *22*, 18564−18578.
(75) Zhang, W.; Wu, T.; Wang, R.; Zhang, X. Surface-Enhanced Circular Dichroism of Oriented Chiral Molecules by Plasmonic Nanostructures. *J. Phys. Chem. C* **2017**, *121*, 666−675.
(76) Govorov, A. O.; Fan, Z. Theory of Chiral Plasmonic Nanostructures Comprising Metal Nanocrystals and Chiral Molecular Media. *ChemPhysChem* **2012**, *13*, 2551−2560.
(77) Doost, M. B.; Langbein, W.; Muljarov, E. A. Resonant-state Expansion Applied to Three-Dimensional Open Optical Systems. *Phys. Rev. A* **2014**, *90*, 013834.
(78) Muljarov, E. A.; Weiss, T. Resonant-state Expansion for Open Optical Systems: Generalization to Magnetic, Chiral, and Bi-Anisotropic Materials. *Opt. Lett.* **2018**, *43*, 1978−1981.
(79) Lobanov, S. V.; Langbein, W.; Muljarov, E. A. Resonant-State Expansion of Three-Dimensional Open Optical Systems: Light Scattering. *Phys. Rev. A* **2018**, *98*, 033820.
(80) Zschiedrich, L.; Binkowski, F.; Nikolay, N.; Benson, O.; Kewes, G.; Burger, S. Riesz-Projection-Based Theory of light−matter Interaction in Dispersive Nanoresonators. *Phys. Rev. A* **2018**, *98*, 043806.
(81) Weiss, T.; Mesch, M.; Schäferling, M.; Giessen, H.; Langbein, W.; Muljarov, E. A. From Dark to Bright: First-Order Perturbation Theory with Analytical Mode Normalization for Plasmonic Nano-antenna Arrays Applied to Refractive Index Sensing. *Phys. Rev. Lett.* **2016**, *116*, 237401.
(82) Weiss, T.; Muljarov, E. A. How to Calculate the Pole Expansion of the Optical Scattering Matrix from the Resonant States. *Phys. Rev. B* **2018**, *98*, 085433.
(83) Both, S.; Weiss, T. Resonant States and Their Role in Nanophotonics. *Semicond. Sci. Technol.* **2022**, *37*, 013002.
(84) Yang, J.; Giessen, H.; Lalanne, P. Simple Analytical Expression for the Peak-Frequency Shifts of Plasmonic Resonances for Sensing. *Nano Lett.* **2015**, *15*, 3439−3444.
(85) Lalanne, P.; Yan, W.; Vynck, K.; Sauvan, C.; Hugonin, J.-P. Light Interaction with Photonic and Plasmonic Resonances. *Laser & Photonics Reviews* **2018**, *12*, 1700113.
(86) Yan, W.; Faggiani, R.; Lalanne, P. Rigorous Modal Analysis of Plasmonic Nanoresonators. *Phys. Rev. B* **2018**, *97*, 205422.
(87) Kamandar Dezfouli, M.; Hughes, S. Regularized Quasinormal Modes for Plasmonic Resonators and Open Cavities. *Phys. Rev. B* **2018**, *97*, 115302.
(88) Kristensen, P. T.; Herrmann, K.; Intravaia, F.; Busch, K. Modeling Electromagnetic Resonators Using Quasinormal Modes. *Adv. Opt. Photon.* **2020**, *12*, 612−708.
(89) Johnson, S. G.; Ibanescu, M.; Skorobogatiy, M. A.; Weisberg, O.; Joannopoulos, J. D.; Fink, Y. Perturbation Theory for Maxwell's Equations with Shifting Material Boundaries. *Phys. Rev. E* **2002**, *65*, 066611.
(90) Unger, A.; Kreiter, M. Analyzing the Performance of Plasmonic Resonators for Dielectric Sensing. *J. Phys. Chem. C* **2009**, *113*, 12243−12251.
(91) Zhang, W.; Martin, O. J. F. A Universal Law for Plasmon Resonance Shift in Biosensing. *ACS Photonics* **2015**, *2*, 144−150.
(92) Sauvan, C.; Hugonin, J. P.; Maksymov, I. S.; Lalanne, P. Theory of the Spontaneous Optical Emission of Nanosize Photonic and Plasmon Resonators. *Phys. Rev. Lett.* **2013**, *110*, 237401.
(93) Lalanne, P.; et al. Quasinormal Mode Solvers for Resonators with Dispersive Materials. *J. Opt. Soc. Am. A* **2019**, *36*, 686−704.
(94) Vial, B.; Zolla, F.; Nicolet, A.; Commandré, M. Quasimodal Expansion of Electromagnetic Fields in Open Two-Dimensional Structures. *Phys. Rev. A* **2014**, *89*, 023829.
(95) Muljarov, E. A.; Langbein, W.; Zimmermann, R. Brillouin-Wigner Perturbation Theory in Open Electromagnetic Systems. *EPL* **2010**, *92*, 50010.
(96) Zhang, H.; Miller, O. D. Quasinormal Coupled Mode Theory. *arXiv*, 2010.08650, 2020; https://arxiv.org/abs/2010.08650 (accessed November 25, 2020).
(97) Weiss, T.; Schäferling, M.; Giessen, H.; Gippius, N. A.; Tikhodeev, S. G.; Langbein, W.; Muljarov, E. A. Analytical Normalization of Resonant States in Photonic Crystal Slabs and Periodic Arrays of Nanoantennas at Oblique Incidence. *Phys. Rev. B* **2017**, *96*, 045129.
(98) Both, S.; Weiss, T. First-Order Perturbation Theory for Changes in the Surrounding of Open Optical Resonators. *Opt. Lett.* **2019**, *44*, 5917−5920.
(99) Alpeggiani, F.; Parappurath, N.; Verhagen, E.; Kuipers, L. Quasinormal-Mode Expansion of the Scattering Matrix. *Phys. Rev. X* **2017**, *7*, 021035.
(100) Doost, M. B.; Langbein, W.; Muljarov, E. A. Resonant state Expansion Applied to Two-Dimensional Open Optical Systems. *Phys. Rev. A* **2013**, *87*, 043827.
(101) Lobanov, S. V.; Zoriniants, G.; Langbein, W.; Muljarov, E. A. Resonant-state Expansion of Light Propagation in Nonuniform Waveguides. *Phys. Rev. A* **2017**, *95*, 053848.
(102) Neale, S.; Muljarov, E. A. Resonant-State Expansion For Planar Photonic Crystal Structures. *Phys. Rev. B* **2020**, *101*, 155128.
(103) Martin, O. J. F.; Piller, N. B. Electromagnetic Scattering in Polarizable Backgrounds. *Phys. Rev. E* **1998**, *58*, 3909−3915.
(104) de Lasson, J. R.; Mørk, J.; Kristensen, P. T. Three-Dimensional Integral Equation Approach to Light Scattering, Extinction Cross Sections, Local Density of States, and Quasi-Normal Modes. *J. Opt. Soc. Am. B* **2013**, *30*, 1996−2007.
(105) Yang, J.; Hugonin, J.-P.; Lalanne, P. Near-to-Far Field Transformations for Radiative and Guided Waves. *ACS Photonics* **2016**, *3*, 395−402.
(106) Schäferling, M.; Giessen, H. Comment on "Enantioselective Optical Trapping of Chiral Nanoparticles with Plasmonic Tweezers. *ACS Photonics* **2018**, *5*, 2533−2534.
(107) Jackson, J. D. *Classical Electrodynamics*, 3rd ed.; Wiley: New York, NY, 1999.
(108) Gansel, J. K.; Thiel, M.; Rill, M. S.; Decker, M.; Bade, K.; Saile, V.; von Freymann, G.; Linden, S.; Wegener, M. Gold Helix Photonic Metamaterial as Broadband Circular Polarizer. *Science* **2009**, *325*, 1513−1515.
(109) Kaschke, J.; Wegener, M. Gold Triple-Helix Mid-Infrared Metamaterial by STED-Inspired Laser Lithography. *Opt. Lett.* **2015**, *40*, 3986−3989.
(110) Tang, Y.; Cohen, A. E. Enhanced Enantioselectivity in Excitation of Chiral Molecules by Superchiral Light. *Science* **2011**, *332*, 333−336.
(111) Rayleigh, L. Note on the Remarkable Case of Diffraction Spectra Described by Prof. Wood. *Philos. Mag., Series 1* **1907**, *14*, 60−65.
(112) Liu, N.; Guo, H.; Fu, L.; Kaiser, S.; Schweizer, H.; Giessen, H. Three-Dimensional Photonic Metamaterials at Optical Frequencies. *Nat. Mater.* **2008**, *7*, 31−37.
(113) Weiss, T.; Granet, G.; Gippius, N. A.; Tikhodeev, S. G.; Giessen, H. Matched Coordinates and Adaptive Spatial Resolution in The Fourier Modal Method. *Opt. Express* **2009**, *17*, 8051−8061.

https://doi.org/10.1021/acsnano.1c09796
ACS Nano 2022, 16, 2822−2832